Transmission Electron Microscopic Study of the Defect Structure in $Sr_4Fe_6O_{12+\delta}$ Compounds with Variable Oxygen Content

Marta D. Rossell,[†] Artem M. Abakumov,[‡] Gustaaf Van Tendeloo,*,[†] Marat V. Lomakov,[‡]
Sergey Ya. Istomin,[‡] and Evgeny V. Antipov[‡]

Electron Microscopy for Material Science (EMAT), University of Antwerp, Groenenborgerlaan 171,
B-2020, Antwerp, Belgium, and Department of Chemistry, Moscow State University,
Moscow 119992, Russia

$Sr_4Fe_6O_{12+\delta}$ ($\delta = 0.6, 0.8$) compounds were prepared by a solid-state reaction in evacuated sealed silica tubes. The structure of these materials was studied by X-ray powder diffraction, electron diffraction, and high-resolution electron microscopy. The materials are characterized as a complicated superstructure appearing at three different levels: (a) modulations with $\mathbf{q} = \alpha\mathbf{a}*$ due to changing δ, so that $\delta = 2\alpha$; (b) cooperative atomic displacements in the $Fe_2O_{2+\delta}$ layers resulting in the formation of distorted tetragonal pyramids and distorted trigonal bipyramids around the Fe cations; and (c) different stackings of neighboring $Fe_2O_{2+\delta}$ layers. Symmetry changes occurring at each of these three levels are discussed. A comparison is made between the $Sr_4Fe_6O_{12+\delta}$ structures in bulk and in thin film.

1. Introduction

The current interest in layered perovskite-like phases based on the $Sr_4Fe_6O_{13}$ crystal structure arises from their mixed oxygen and electron conductivity, potentially useful for technological applications such as oxygen separation membranes and electrodes in solid oxide fuel cells. The $Sr_4Fe_6O_{13}$ compound was first prepared by Kanamaru et al.[1] The crystal structure was described by use of the acentric *Iba*2 space group with lattice parameters $a = 11.103(4)$ Å, $b = 18.924(4)$ Å, and $c = 5.572(2)$ Å.[2] The structure is built up of SrO and FeO_2 perovskite-type layers alternating along the *b*-direction with $Fe_2O_{2.5}$ layers of five-coordinated iron polyhedra (Figure 1). Two nonequivalent sites of iron atoms with nearly trigonal bipyramidal or nearly square pyramidal oxygen coordination were found in the $Fe_2O_{2.5}$ layers.[2] The oxygen deficiency in $Sr_4Fe_6O_{13}$ was considered to appear only if this compound was subjected to treatment under strongly reductive conditions. Substantial oxygen deficit corresponding to the $Sr_4Fe_6O_{12.55}$ composition was achieved by postannealing treatment of the as-prepared $Sr_4Fe_6O_{13}$ sample at 1173 K at $p(O_2) = 10^{-12}$ Pa (N_2-H_2 mixture).[3] Oxygen excess samples with compositions $Sr_4Fe_6O_{13.14}$[3] and $Sr_4Fe_6O_{13.41}$[4] can also be prepared by treatment at oxidizing conditions. By use of neutron powder diffraction it was determined that the anion deficiency occurs due to partial occupation of the anion positions in the $Fe_2O_{2.5}$ layers, but

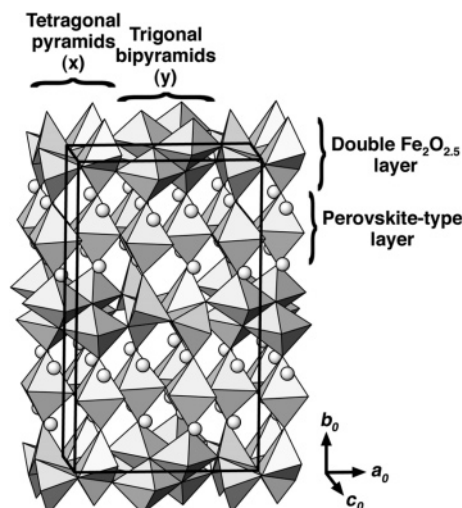**Figure 1.** Three-dimensional view of the $Sr_4Fe_6O_{13}$ crystal structure showing the perovskite-type layers and the $Fe_2O_{2.5}$ layers. The square pyramidal (*x*) and trigonal bipyramidal (*y*) sites of iron atoms are outlined. Shaded circles represent Sr ions.

no long-range order of anion vacancies was detected.[5] Mitchell et al.[6] observed strong discrepancies between the neutron and X-ray synchrotron powder diffraction patterns of their $Sr_4Fe_6O_{13-y}$ sample and the crystal structure of $Sr_4Fe_6O_{13}$ determined by Yoshiasa et al.[2] because of the presence of reflections violating the body-centered unit cell. However, Mitchell et al.[6] did not reveal a possible origin for this symmetry lowering.

Recently, we demonstrated that anion-deficient derivatives of the $Sr_4Fe_6O_{13}$ compound can be prepared as epitaxial thin

* Corresponding author: telephone +32 3 265 3262; fax +32 3 265 3257; e-mail staf.vantendeloo@ua.ac.be.
† University of Antwerp.
‡ Moscow State University.

(1) Kanamaru, F.; Shimada, M.; Koizumi, M. *J. Phys. Chem. Solids* **1972,** *33,* 1169.
(2) Yoshiasa, A.; Ueno, K.; Kanamaru, F.; Horiuchi, H. *Mater. Res. Bull.* **1986,** *21,* 175.
(3) Waerenborgh, J. C.; Avdeev, M.; Patrakeev, M. V.; Kharton, V. V.; Frade, J. R. *Mater. Lett.* **2003,** *57,* 3245.
(4) Guggilla, S.; Manthiram, A. *J. Electrochem. Soc.* **1997,** *144,* L120.
(5) Avdeev, M. Y.; Patrakeev, M. V.; Kharton, V. V.; Frade, J. R. *J. Solid State Electrochem.* **2002,** *6,* 217.
(6) Mitchell, B. J.; Richardson, J. W., Jr.; Murphy, C. D.; Ma, B.; Balachandran, U.; Hodges, J. P.; Jorgensen, J. D. *J. Eur. Ceram. Soc.* **2002,** *22,* 661.
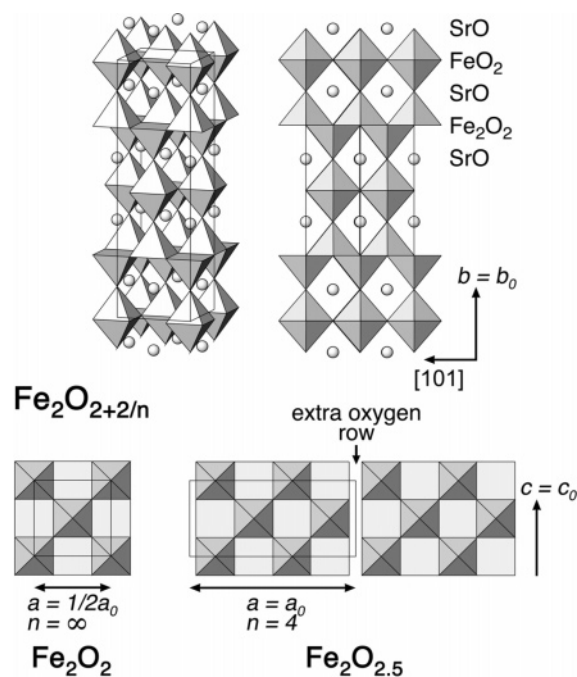
Figure 2. Top: average $Sr_4Fe_6O_{12}$ structure and its [$\bar{1}01$] projection. Bottom: schematic representation of the formation of the $Fe_2O_{2+2/n}$ layers for $n = \infty$ (average structure, Fe_2O_2 layers) and $n = 4$ ($Sr_4Fe_6O_{13}$ structure, $Fe_2O_{2.5}$ layers). The FeO_5 square pyramids pointing above and below the layer plane are shown.

films grown by a pulsed laser deposition (PLD) technique under reducing conditions on single-crystal $SrTiO_3$ substrates. The anion-deficient thin films with a tentative $Sr_4Fe_6O_{12.8}$ composition were obtained at much softer reductive conditions [$T = 1023$ K, $p(O_2) = 3 \times 10^{-2}$ mbar] being applied in situ at the preparation, compared with the conditions necessary to reduce the as-prepared $Sr_4Fe_6O_{13}$ by postannealing.[7,8] The structure of the anion-deficient material was deduced from electron diffraction (ED) and high-resolution electron microscopy (HREM).[8] In contrast to the compounds reduced by postannealing, oxygen atoms and vacancies in the $Sr_4Fe_6O_{12.8}$ are placed in an ordered manner. A generalized description of the $Sr_4Fe_6O_{12+\delta}$ phases was proposed on the basis of the possibilities of the $(3 + 1)$D crystallography. The average structure of the $Sr_4Fe_6O_{12+\delta}$ phases was built by use of the face-centered orthorhombic unit cell with $a = a_p\sqrt{2} = {}^1\!/_2 a_0$, $b = 4a_p = b_0$, $c = a_p\sqrt{2} = c_0$ (where a_p is the parameter of the perovskite subcell and a_0, b_0, and c_0 are the lattice parameters of the body-centered orthorhombic unit cell of $Sr_4Fe_6O_{13}$). This idealized $Sr_4Fe_6O_{12}$ structure is described as a layer sequence $-SrO-FeO_2-SrO-Fe_2O_2-SrO-$, alternating along the b axis (Figure 2, top). The SrO and FeO_2 layers are identical to the AO and BO_2 layers of the ABO_3 perovskite structure. The Fe_2O_2 layer represents a fragment of the NaCl structure and consists of edge-sharing oxygen squares centered with the Fe atoms. Oxygen atoms from two neighboring SrO layers complete the coordination environment of the Fe atoms in the Fe_2O_2 layers up to a square pyramid. The apical vertexes of the square pyramids are directed up and down, forming a chessboard pattern. The

infinite sequence of the square pyramids along the a axis can be broken by the appearance of extra oxygen rows along the c axis. The extra oxygen rows create bands with a width of n FeO_5 pyramids along the a axis, and the composition of the layer can be calculated as $Fe_2O_{2+2/n}$ resulting in the $Sr_4Fe_6O_{12+4/n}$ phase composition (Figure 2, bottom). The extra oxygen rows alternate in an ordered manner along the a axis, resulting in the appearance of satellite reflections corresponding to a modulation vector $\mathbf{q} = \alpha\mathbf{a}^*$. The thickness n of the bands is then directly related to the α component of the modulation vector as $n = 2/\alpha$. This results in a compound composition $Sr_4Fe_6O_{12+\delta}$ with $\delta = 2\alpha$.

One may expect that in stressed $Sr_4Fe_6O_{12+\delta}$ films, due to the lattice mismatch between the film and the substrate, strain may stabilize certain ordered modulated structures, thus affecting the oxygen content. As an attempt to evaluate the contribution of this mechanism to the strain relaxation, Santiso et al.[9] studied the behavior of the modulation vector in films with thickness ranging from 20 to 300 nm by means of X-ray diffraction. The oxygen content in the films varied with the strain, indicating that the modulation actively participates in the strain relaxation. The thinner fully strained films showed small α values ($\alpha \approx 0.41$), whereas for the thicker partially strained films $\alpha \approx 0.44$.

To clarify how relevant the lattice strain is for the stabilization of a particular $Sr_4Fe_6O_{12+\delta}$ ($\delta < 1$) structure, and driven by the assumption that ordered $Sr_4Fe_6O_{12+\delta}$ phases with different δ values can be prepared if the reductive conditions are applied in situ during the preparation, we have performed the synthesis of bulk $Sr_4Fe_6O_{12+\delta}$ ($\delta < 1$) samples. A similar attempt was recently made by Mellenne et al.,[10] who revisited the synthesis and crystal structure of the Sr_4-Fe_6O_{13} phase in air, nitrogen, and argon. By means of transmission electron microscopy (TEM) they observed modulated structures similar to the ones found earlier in thin films of $Sr_4Fe_6O_{12+\delta}$.[8]

The main difference between the synthesis of Mellenne et al.[10] and the present work is that we have performed the synthesis in evacuated sealed silica tubes starting from initial mixtures with a predefined oxygen deficit in comparison with the $Sr_4Fe_6O_{13}$ composition. This allowed us to observe a wide range of structures with different oxygen content using electron diffraction and high-resolution electron microscopy. The aim of the present paper is to investigate the microstructure and the defect structure of the modulated $Sr_4Fe_6O_{12+\delta}$ phases and broaden our knowledge of the crystal chemistry of these phases.

2. Experimental Section

The $Sr_4Fe_6O_{12+\delta}$ ($\delta = 0.6, 0.8$) samples were prepared by a solid-state reaction in evacuated sealed silica tubes. SrO, Fe_2O_3, and metallic Fe were used as the initial materials. SrO was prepared by decomposition of $SrCO_3$ at 900 °C in a dynamic vacuum of 10^{-3} mbar. Sample preparation was performed in an Ar-filled glovebox. The initial materials were mixed according to the required

(7) Pardo, J. A.; Santiso, J.; Solís, C.; Garcia, G.; Figueras, A.; Rossell, M. D.; Van Tendeloo, G. *J. Cryst. Growth* **2004**, *262*, 334.

(8) Rossell, M. D.; Abakumov, A. M.; Van Tendeloo, G.; Pardo, J. A.; Santiso, J. *Chem. Mater.* **2004**, *16*, 2578.

(9) Santiso, J.; Pardo, J. A.; Solís, C.; Garcia, G.; Figueras, A.; Rossell, M. D.; Van Tendeloo, *Appl. Phys. Lett.* **2005**, *86*, 132105.

(10) Mellenne, B.; Retoux, R.; Lepoittevin, C.; Hervieu, M.; Raveau, B. *Chem. Mater.* **2004**, *16*, 5006.

Table 1. Three-Dimensional Space Groups of the Superstructures Obtained for Different t and Rational α Values[a]

$\alpha = i/j$	$t = \nu/2j$	$t = (2\nu + 1)/4j$	general t
$\alpha = 0$	*Bba*2 [41: *bac̄*]	*Bma*2 [39: *bac̄*]	*Bc* [7: $^{1}/_{2}(\boldsymbol{a} - \boldsymbol{c})\,\boldsymbol{b}\,^{1}/_{2}(\boldsymbol{a} + \boldsymbol{c})$]
j = even	*Ima*2 [46]	*Iba*2 [45]	*Ic* [9: $-(\boldsymbol{a} + \boldsymbol{c})\,\boldsymbol{b}\,\boldsymbol{a}$)]
j = odd; i = even	*Bba*2 [41: *bac̄*]	*Bma*2 [39: *bac̄*]	*Bc* [7: $^{1}/_{2}(\boldsymbol{a} - \boldsymbol{c})\,\boldsymbol{b}\,^{1}/_{2}(\boldsymbol{a} + \boldsymbol{c})$]
j = odd; i = odd	*Ccc*2 [37]	*Cmc*2₁ [36]	*Cc* [9]
$\alpha = 1$	*Ccc*2 [37]	*Cmc*2₁ [36]	*Cc* [9]

[a] i, j, ν = integer.

cation ratio and oxygen content and placed into alumina crucibles and then into silica tubes, which were evacuated up to a residual pressure of 10^{-2} mbar and sealed. The samples were annealed at 1000 °C for 48 h. After furnace cooling, the tubes were opened, the samples were reground and pressed into pellets, the tubes were sealed, and the samples were annealed again at 1000 °C for 48 h. Finally the samples were furnace-cooled.

Phase analysis and cell parameter determination were performed by X-ray powder diffraction (XRPD) with a Huber G670 Guinier diffractometer (Cu Kα1-radiation, image plate detector).

Electron diffraction (ED) and high-resolution electron microscopy (HREM) investigations were performed on crushed samples deposited on holey carbon grids. ED patterns were obtained on a Philips CM20 microscope, while HREM observations were performed on a JEOL 4000EX microscope, with a Scherzer resolution of 0.17 nm. Image simulations were made with the MacTempas software. NIH Image 1.60 software was used for image processing.

3. Results and Discussion

3.1. General Considerations. A general crystallographic approach to the structures of the $Sr_4Fe_6O_{12+\delta}$ materials with different δ values can be developed by starting from the significantly simplified average $Sr_4Fe_6O_{12}$ structure, which is described briefly in the Introduction and more thoroughly considered in ref 8. The complicated structural behavior of the $Sr_4Fe_6O_{12+\delta}$ phases is related to the changes occurring in the NaCl-type $Fe_2O_{2+\delta}$ layers upon changing δ. These changes are at the origin of superstructure formation at three different levels:

(i) The periodicity along the a axis changes with respect to the amount of extra oxygen rows in the $Fe_2O_{2+\delta}$ layers and their ordered alternation pattern, which breaks the infinite layer into a sequence of bands of FeO₅ tetragonal pyramids. The bands of different thickness run along the c axis and alternate along the a axis, creating a periodicity corresponding to a modulation vector $\mathbf{q} = \alpha\mathbf{a}^*$. The thickness n (number of FeO₅ pyramids) of the bands is then directly related to the α component of the modulation vector as $n = 2/\alpha = 4/\delta$.

(ii) The iron and oxygen atoms in the $Fe_2O_{2+\delta}$ layers are subject to cooperative displacements that transform the idealized tetragonal FeO₅ pyramids into distorted tetragonal pyramids and distorted trigonal bipyramids. Within a band of thickness n there is only one subband of tetragonal pyramids with a thickness x and one subband of the trigonal bipyramids with a thickness y, so that $n = x + y$.

(iii) Neighboring $Fe_2O_{2+\delta}$ layers separated by $^{1}/_{2}b$ can be shifted with respect to each other by a lattice translation of the average structure, resulting in different mutual arrangements and, consequently, different polytypes.

From our previous investigations of $Sr_4Fe_6O_{12+\delta}$ thin films, we have derived the $(3 + 1)$D superspace group for the

modulated $Sr_4Fe_6O_{12+\delta}$ structures to be $Xmmm(\alpha00)0s0$, where X stands for the conventional basis with centering vectors $(0, ^{1}/_{2}, ^{1}/_{2}, ^{1}/_{2})$, $(^{1}/_{2}, 0, ^{1}/_{2}, 0)$, and $(^{1}/_{2}, ^{1}/_{2}, 0, ^{1}/_{2})$. Being transformed into a primitive basis, this corresponds to the superspace group $Fmmm(\alpha10)0s0$, so that $\mathbf{q} = \alpha\mathbf{a}^* + \mathbf{b}^*$. The superspace symmetry has to be adopted in order to fit the only reliable refined structure of the compounds of the $Sr_4Fe_6O_{12+\delta}$ series, namely, $Sr_4Fe_6O_{13}$. This structure represents the commensurate case with a modulation vector $\mathbf{q} = ^{1}/_{2}\mathbf{a}^*$ and a noncentrosymmetric 3D space group Iba2.[2] Thus the noncentrosymmetric subgroup $Xmm2(\alpha00)0s0$ [$Fmm2(\alpha10)0s0$ in a primitive basis] was further used to determine possible 3D space symmetries for the *commensurately* modulated structures, arising from the first level of the superstructure. For the *commensurately* modulated structure, the actual 3D space group of the superstructure depends on the choice of the initial "phase" of the modulation t (the underlying theory is briefly described in the International Tables for Crystallography[11]). For different choices of t, the 3D space group is derived from the $(3 + 1)$D space group by restricting it to a subgroup that leaves the physical 3D space invariant. The analysis of 3D symmetries for rational α components of the modulation vector and some particular and general values of t is given in Table 1. One can see that the space group Iba2, experimentally found for the $Sr_4Fe_6O_{13}$ crystal structure, is present in this table and corresponds to the case with $\alpha = ^{1}/_{2}$ and $t = (2\nu + 1)/8$ (ν = integer). The space group Bba2 proposed earlier for the $Sr_4Fe_6O_{12.8}$ structure model with $\alpha = ^{2}/_{5}$ is also present among the space groups derived from the $(3 + 1)$D symmetry ($t = \nu/10$).

Several important conclusions can be made from the symmetry analysis described above. First of all, it allows us to build a feasible structure model explaining anion overstoichiometry in comparison with the $Sr_4Fe_6O_{13}$ composition. The limiting case of $\alpha = 1$ corresponds to $n = 2$ and the $Sr_4Fe_6O_{14}$ composition with possible space symmetries Ccc2, Cmc2₁, and Cc. Considering the second level of the superstructure (formation of distorted tetragonal pyramids and trigonal bipyramids), only the case of $x = y = 1$ is possible, which can be realized in the frame of the Cmc2₁ space group, resulting in the structure model shown in Figure 3. The oxidation state of iron in this tentative structure is equal to +3.33, and strong oxidative conditions should be applied for the preparation of this compound in a pure form. However, the presence of defects or local areas corresponding to the $Sr_4Fe_6O_{14}$ structure are a plausible explanation for the insertion of a rather large amount of extra oxygen into $Sr_4Fe_6O_{12+\delta}$ (up to $\delta = 1.41$).[4] An alternative possibility is the

(11) *International Tables for Crystallography*; Kluwer Academic Publishers: London, 1999; Vol. C, p 899.

Table 2. Oxygen Content, Cell Parameters, 3D Space Group,[a] α Component of Modulation Vector q = αa*, and Distribution of Bands[b]

oxygen content (12+δ)	tentative oxidation state of Fe	lattice parameters			space group	α component of modulation vector $\mathbf{q} = \alpha a^*$	n = x:y
		a	b	c			
12 (δ = 0) (tentative basic structure)	2.67	$a_p\sqrt{2}$	$\sim 4a_p$	$a_p\sqrt{2}$	$Fmmm$ [69]	0	∞
12.67 (δ = 2/3)	2.89	$\sim 3a_p\sqrt{2}$	$\sim 4a_p$	$\sim a_p\sqrt{2}$	$Cmc2_1$ [36]	$^1/_3$	6 = 3:3
12.80 (δ = 4/5)	2.93	$\sim 5a_p\sqrt{2}$	$\sim 4a_p$	$\sim a_p\sqrt{2}$	$Bba2$ [41:$ba\bar{c}$]	$^2/_5$	5 = 2:3
13 (δ = 1)	3.00	$\sim 2a_p\sqrt{2}$	$\sim 4a_p$	$\sim a_p\sqrt{2}$	$Iba2$ [45]	$^1/_2$	4 = 2:2
14 (δ = 2) (hypothetical fully oxidized phase)	3.33	$\sim a_p\sqrt{2}$	$\sim 4a_p$	$\sim a_p\sqrt{2}$	$Cmc2_1$ [36]	1	2 = 1:1

[a] As derived from the (3 + 1)D superspace group $Xmm2(\alpha00)0s0$ with centering vectors $(0, ^1/_2, ^1/_2, ^1/_2)$, $(^1/_2, 0, ^1/_2, 0)$, and $(^1/_2, ^1/_2, 0, ^1/_2)$. [b] Distribution of bands of n FeO$_5$ pyramids into distorted tetragonal pyramids (x) and distorted trigonal bipyramids (y) of Sr$_4$Fe$_6$O$_{12+\delta}$.
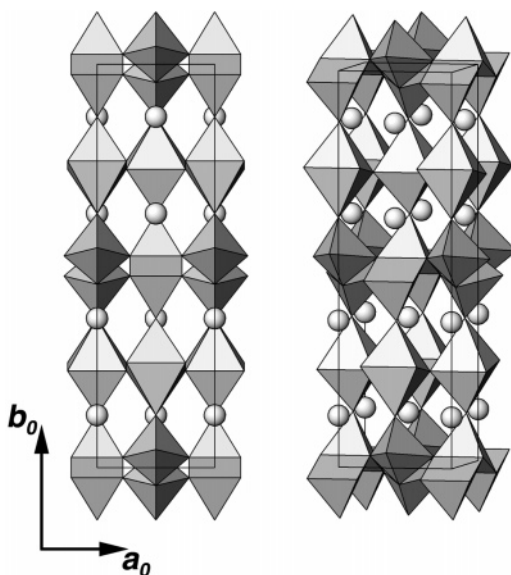

Figure 3. Model of the anion-excess Sr$_4$Fe$_6$O$_{14}$ crystal structure: [001] projection and 3D view. The Fe atoms are at the octahedral, trigonal bipyramidal, and square pyramidal sites. Shaded circles represent Sr ions.

Figure 4. X-ray powder diffraction pattern of the Sr$_4$Fe$_6$O$_{12.8}$ sample. The reflection indexes are marked according to a face-centered orthorhombic unit cell with $^1/_2a_0$, b_0, c_0.

formation of modulated structures with α > $^1/_2$, for example, α ≈ 0.7 for δ = 1.41. A summarizing table with the oxygen content, lattice parameters, space group as derived from the (3 + 1)D superspace group $Xmm2(\alpha00)0s0$ with centering vectors $(0, ^1/_2, ^1/_2, ^1/_2)$, $(^1/_2, 0, ^1/_2, 0)$, and $(^1/_2, ^1/_2, 0, ^1/_2)$, the α component of the modulation vector $\mathbf{q} = \alpha a^*$, and the distribution of bands of n FeO$_5$ pyramids into distorted tetragonal pyramids (x) and distorted trigonal bipyramids (y) of the Sr$_4$Fe$_6$O$_{12+\delta}$ compounds is given in Table 2.

This clear interdependence of the space symmetry and the oxygen nonstoichiometry can clarify the discrepancies between the neutron and X-ray synchrotron powder diffraction patterns observed by Mitchell et al.[6] on their Sr$_4$Fe$_6$O$_{13-y}$ sample and the crystal structure of Sr$_4$Fe$_6$O$_{13}$ determined by Yoshiasa et al.[2] Indeed, the violation of the I-centering observed by Mitchell et al.[6] can be attributed to the symmetry lowering due to a variation of the oxygen content. Unfortunately, Mitchell et al.[6] did not measure the oxygen content in their sample and did not report a structure refinement.

The space symmetries of the Sr$_4$Fe$_6$O$_{12+\delta}$ phases derived from the (3 + 1)D space group can be compared with those described by Mellenne et al.;[10] moreover, these have to be critically reevaluated. The most symmetric unit cell proposed by Mellenne et al.[10] is orthorhombic C-centered for α = $^1/_2$, $^1/_3$, $^1/_4$, ..., and monoclinic for α = $^2/_5$, $^2/_7$, $^2/_9$, ... This proposal is in contradiction with the $Iba2$ space symmetry experimentally determined from single-crystal X-ray diffraction data for α = $^1/_2$[2] and with the structural model of the Sr$_4$-
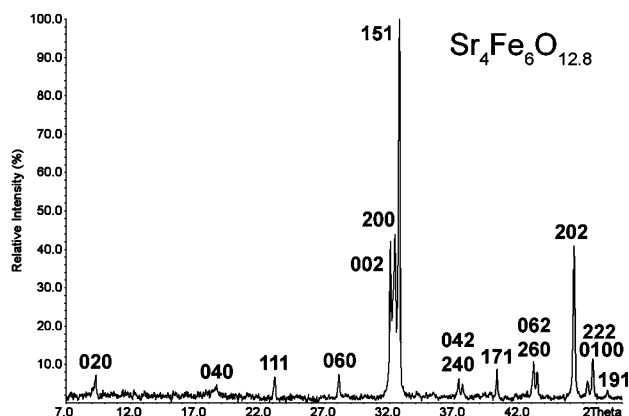
Fe$_6$O$_{12.8}$ phase (α = $^2/_5$) with $Bba2$ space symmetry as confirmed by HREM observations.[8] According to Table 1, the space symmetry for α = $^1/_2$, $^1/_4$, $^1/_6$, ... and for α = $^2/_5$, $^2/_7$, $^2/_9$, ... can be higher than that proposed by Mellenne et al.[10]

It should be noted that the space symmetries given in Table 1 can be reduced down to the corresponding subgroups due to different ordered patterns of the subbands of the tetragonal pyramids and trigonal bipyramids and a different stacking sequence of the Fe$_2$O$_{2+\delta}$ layers along the b axis, that is, the appearance of second- and third-level superstructures. This will be illustrated below by TEM observations of anion ordering in the Sr$_4$Fe$_6$O$_{12+\delta}$ phases.

3.2. X-ray Diffraction Study. XRPD patterns of the Sr$_4$-Fe$_6$O$_{12+\delta}$ (δ = 0.6, 0.8) samples (Figure 4, for δ = 0.8) show a strong resemblance to the XRPD pattern of Sr$_4$Fe$_6$O$_{13}$ calculated from the structural data from ref 2. The intensity distribution of the main reflections does not change significantly when the oxygen content is changed, which reflects that the cation sublattice remains roughly unaltered. At the same time, the reflections with h = even vanish completely on the XRPD patterns. The XRPD patterns of Sr$_4$Fe$_6$O$_{12+\delta}$ (δ = 0.6, 0.8) can be completely indexed with a face-centered orthorhombic unit cell with $a = ^1/_2a_0$, $b = b_0$, and $c = c_0$ (where a_0, b_0, and c_0 are the lattice parameters of the body-centered orthorhombic unit cell of Sr$_4$Fe$_6$O$_{13}$). The unit cell determined from the XRPD patterns coincides with that proposed for the average Sr$_4$Fe$_6$O$_{12}$ parent structure. The absence of reflections responsible for an increase of the repeat period along the a axis on the XRPD patterns of the Sr$_4$-Fe$_6$O$_{12+\delta}$ (δ = 0.6, 0.8) samples can be related to a high degree of disorder in the oxygen sublattice.

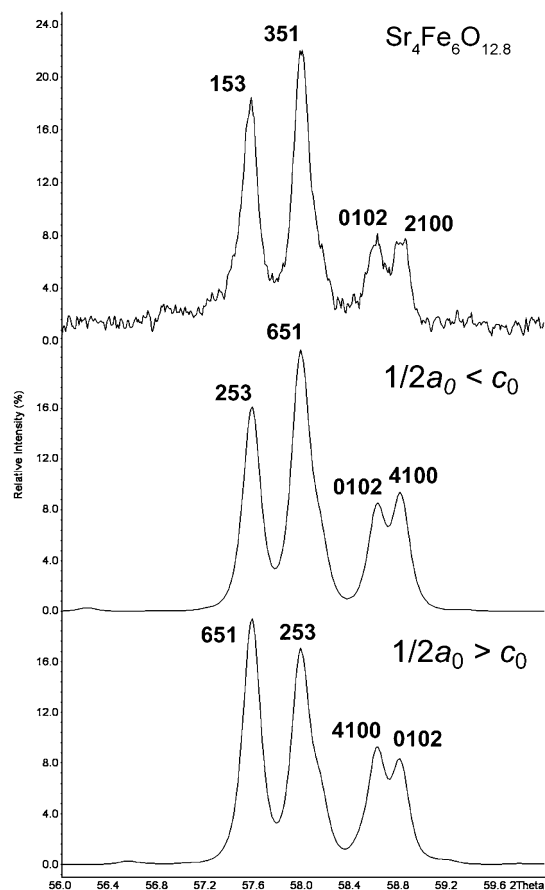The Sr$_4$Fe$_6$O$_{12+\delta}$ samples exhibit a remarkable increase of the orthorhombic distortion with respect to the perovskite

Figure 5. Part of the X-ray powder diffraction pattern of the Sr$_4$Fe$_6$O$_{12.8}$ sample (top) along with the patterns calculated from the Sr$_4$Fe$_6$O$_{13}$ structure data for the settings $^1/_2a_0 < c_0$ (middle) and $^1/_2a_0 > c_0$ (bottom). The reflections are indexed according to the $^1/_2a_0$, b_0, c_0 unit cell (top pattern) and the a_0, b_0, c_0 unit cell (middle and bottom patterns).

subcell being compared with the lattice parameters of Sr$_4$Fe$_6$O$_{13}$ as given by Yoshiasa et al.[2] ($^1/_2a_0 = 5.5515$ Å, $b_0 = 18.924$ Å, and $c_0 = 5.572$ Å). For Sr$_4$Fe$_6$O$_{12.8}$ a larger difference between the parameters a and c [$a = 5.5245(2)$ Å, $b = 19.0635(7)$ Å, and $c = 5.5778(2)$ Å] is visible on the XRPD pattern (Figure 4) by a clear splitting of the $0kl$ and $hk0$ reflections. Surprisingly, when comparing the lattice parameters of the Sr$_4$Fe$_6$O$_{12.8}$ sample with the previously published lattice parameters of Sr$_4$Fe$_6$O$_{13}$, we found significant discrepancies between the data provided for the latter by different authors. For the same *Iba*2 setting, a unit cell with $^1/_2a_0 < c_0$ is reported in refs 2, 12, and 13, whereas a unit cell with $^1/_2a_0 > c_0$ is reported in refs 1, 5, 14, and 15. Such discrepancy is probably caused by the small difference between $^1/_2a_0$ and c_0 for the Sr$_4$Fe$_6$O$_{13}$ material, which causes a strong overlap of the basic reflections, and by the small intensity of the reflections responsible for the doubling cell parameter along the a axis. In the case of the Sr$_4$Fe$_6$O$_{12.8}$ phase, this question can be unambiguously resolved due to the larger difference between $^1/_2a_0$ and c_0. Figure 5 shows a part of the experimental XRPD pattern of Sr$_4$Fe$_6$O$_{12.8}$ along

(12) Patrakeev, M. V.; Mitberg, E. B.; Leonidov, I. A.; Kozhevnikov, V. L. *Solid State Ionics* **2001**, *139*, 325.
(13) Ma, B.; Hodges, J. P.; Jorgensen, J. D.; Miller, D. J.; Richardson, J. W.; Balachandran, U. *J. Solid State Chem.* **1998**, *141*, 576.
(14) Guggilla, S.; Armstrong, T.; Manthiram, A. *J. Solid State Chem.* **1999**, *145*, 260.
(15) Tsuchida, T.; Kan, T. *J. Eur. Ceram. Soc.* **2001**, *21*, 555.

with the theoretical XRPD patterns calculated from the atomic coordinates of Sr$_4$Fe$_6$O$_{13}$[2] for the cases of $^1/_2a_0 < c_0$ and $^1/_2a_0 > c_0$. It is easy to see that the pattern calculated with $^1/_2a_0 > c_0$ is in obvious disagreement with the experimental pattern, and thus the $^1/_2a_0 < c_0$ setting must be accepted. This conclusion will be further supported by electron diffraction observations. It is also in agreement with the results of the crystal structure determination of Sr$_4$Fe$_6$O$_{13}$ and Sr$_4$Fe$_4$Co$_2$O$_{13}$,[2,16] which were both performed with the $^1/_2a_0 < c_0$ setting.

One can speculate that the increase in orthorhombic distortion is caused by an increase of the mismatch between the Sr$-$O and Fe$-$O interatomic distances upon a partial reduction of Fe(III) to Fe(II) due to a smaller oxygen content. This mismatch is compensated by a tilting of the FeO$_6$ octahedra in the perovskite block around the a axis. The partial replacement of smaller Fe^{3+} cations ($r = 0.645$ Å, CN = 6) by larger Fe^{2+} ones ($r = 0.77$ Å, CN = 6) results in an expansion of the structure along the b and c axes and a simultaneous contraction of the a parameter because of the larger tilt angle, which compensates the increasing mismatch between the Sr$-$O and Fe$-$O interatomic distances. The decrease of the formal oxidation state of iron is also reflected by an increase of the unit cell volume by 0.35% on going from Sr$_4$Fe$_6$O$_{13}$ to Sr$_4$Fe$_6$O$_{12.8}$.

3.3. Electron Microscopic Study. *3.3.1. Variation of* α *with the Anion Content.* The [001]* ED patterns of the Sr$_4$Fe$_6$O$_{12+\delta}$ phases reflect the main features related to the first level of the superstructure. The indexation of these patterns can be performed with four *hklm* indexes given by diffraction vectors $\mathbf{g} = h\mathbf{a}^* + k\mathbf{b}^* + l\mathbf{c}^* + m\mathbf{q}$, $\mathbf{q} = \alpha\mathbf{a}^*$ in the frame of the proposed superspace group $Xmm2(\alpha 00)0s0$ with centering vectors $(0, ^1/_2, ^1/_2, ^1/_2)$, $(^1/_2, 0, ^1/_2, 0)$, and $(^1/_2, ^1/_2, 0, ^1/_2)$ [$Fmm2(\alpha 10)0s0$ with the modulation vector $\mathbf{q} = \alpha\mathbf{a}^* + \mathbf{b}^*$]. The reflection conditions are *HKLm*: $H + K + m = 2n$, $H + L = 2n$, $K + L + m = 2n$; *H0Lm*, with $m = 2n$. The representative [001]* ED patterns of a *commensurate* superstructure with $\alpha = ^1/_3$ along with two incommensurate cases with $\alpha = 0.36$ and 0.39 are shown in Figure 6. The indexation scheme is presented in Figure 7. The reflections with $m = 0$, which belong to the average structure, match well with a face-centered orthorhombic lattice with cell parameters $a = ^1/_2a_0$, $b = b_0$, and $c = c_0$, in agreement with the XRPD data. The reflections with $m \neq 0$ are the satellites; those positions shift with changing α component and are directly related to the oxygen content. Thus, these reflections are responsible for the first level of the superstructure. The α component varies from one crystallite to another, ranging from 0.33 to 0.39, reflecting local inhomogeneity in the oxygen distribution. It should be noted that the indexation of the ED pattern of the $\alpha = ^1/_3$ commensurate phase can be equally well performed by use of a 3D unit cell with $a = ^3/_2a_0$, $b = b_0$, and $c = c_0$.

Very weak reflections at the positions $\mathbf{g} \pm \mathbf{b}^*$ can be observed at the [001]* ED patterns of the $\alpha = 0.36$ phase (Figure 6). These reflections can be attributed to a further

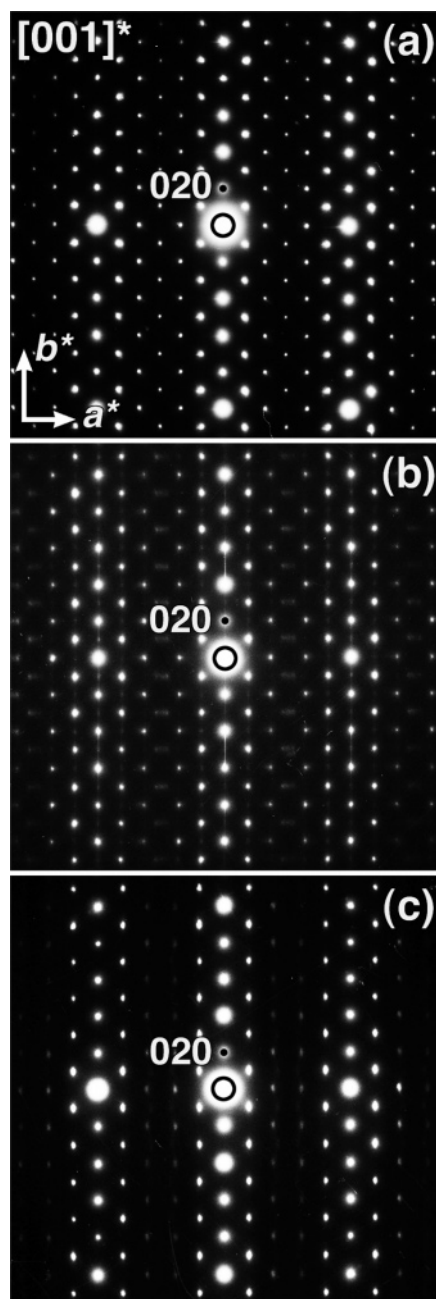(16) Fjellvåg, H.; Hauback, B. C.; Bredesen, R. *J. Mater. Chem.* **1997**, *7*, 2415.

Figure 6. [001]* ED patterns of reduced $Sr_4Fe_6O_{12+\delta}$ compounds with (a) $\alpha = \frac{1}{3}$, (b) $\alpha = 0.36$, and (c) $\alpha = 0.39$.

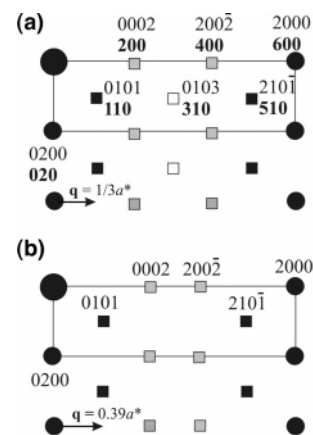**Figure 7.** Indexation schemes of the [001]* ED patterns for $Sr_4Fe_6O_{12+\delta}$ phases with $\alpha = \frac{1}{3}$ (a) and $\alpha = 0.39$ (b). Main reflections and first-, second-, and third-order satellites are marked as circles and black, gray, and white squares, respectively. For the $\alpha = \frac{1}{3}$ phase, the indexes of the commensurate $\frac{3}{2}a_0$, b_0, c_0 supercell are given in boldface type.
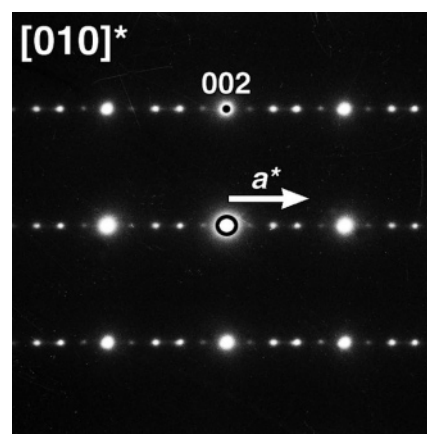

Figure 8. [010]* ED pattern of the commensurately modulated $Sr_4Fe_6O_{12+\delta}$ phase with $\alpha = \frac{2}{5}$.

symmetry decrease due to the appearance of the second and third level of superstructure as it will be discussed below.

Satellite reflections are also observed on the [010]* ED patterns, as shown in Figure 8 for a *commensurate* case with $\alpha = \frac{2}{5}$. In comparison with the $\alpha = 0.39$ phase, the difference in the positions of the satellites along a^* on the [010]* ED pattern of the $\alpha = \frac{2}{5}$ phase is small but clearly detectable. The positions of the satellites match the extinction conditions given above. The indexation scheme for the [010]* ED pattern was described recently.[8] This pattern and similar patterns for other α values allow us to confirm the $\frac{1}{2}a_0 < c_0$ setting used for the indexation of the XRPD patterns of the $Sr_4Fe_6O_{12+\delta}$ phases. Indeed, the absolute values of the interplanar distances cannot be measured from the ED patterns with high accuracy, but the d_{200}/d_{002} ratio can be evaluated more precisely. A $d_{200}/d_{002} = 0.989$ ratio was

measured from the pattern in Figure 8, which is in good agreement with the ratio $d_{200}/d_{002} = 0.990$ obtained from the XRPD data.

Two different [001] HREM images, corresponding to $\alpha = \frac{1}{3}$ and $\alpha = 0.39$ with very similar defocus and thickness conditions, of $Sr_4Fe_6O_{12+\delta}$ and their corresponding Fourier transforms (FT) are shown in Figure 9. The FT pattern of Figure 9c exhibits a spot distribution similar to that of the corresponding ED pattern in Figure 6a, while the FT pattern of Figure 9d is similar to the ED pattern of Figure 6c. The average visible repeat period along the b axis corresponds to the -SrO-FeO$_2$-SrO-Fe$_2$O$_{2+\delta}$-SrO- sequence of alternating layers. From a comparison of the [001] simulated images with the experimental images, dark layers and thicker bright layers correspond to the perovskite-type FeO$_2$ layers and the Fe$_2$O$_{2+\delta}$ layers, respectively. The SrO layers, imaged as continuous rows of bright dots, delimit the two types of layers. In both figures, a well-defined arrangement of the FeO$_5$ trigonal bipyramids and the square pyramids in the Fe$_2$O$_{2+\delta}$ layers along the a direction is clearly observed. For Figure 9a, the observed sequence along the a direction corresponds strictly to a periodicity of 6 FeO$_5$ polyhedra (the $a = \frac{3}{2}a_0$, $b = b_0$ supercell is outlined), in accordance with $\alpha = \frac{1}{3}$. For Figure 9b, the main periodicity of 5 FeO$_5$ polyhedra is systematically violated by 6 FeO$_5$ polyhedra
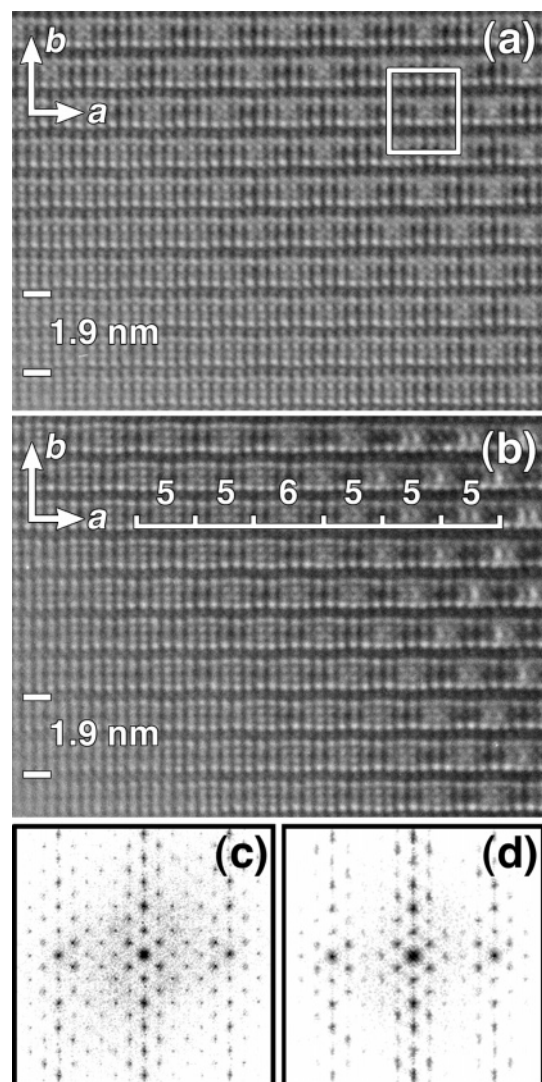
Figure 9. [001] HREM images of $Sr_4Fe_6O_{12+\delta}$ phases showing (a) *commensurate* modulation with $\alpha = {}^1/_3$ and (b) incommensurate modulation with $\alpha = 0.39$; (c, d) corresponding FT patterns of images a and b, respectively. The commensurate $^3/_2a_0$, b_0 supercell is outlined by a white rectangle for $\alpha = {}^1/_3$. White brackets mark the sequence of bands with thicknesses of 5 and 6 FeO_5 polyhedra for $\alpha = 0.39$.

Figure 10. Possible arrangements of FeO_5 polyhedra in the $Fe_2O_{2.33}$ layer of the $Sr_4Fe_6O_{12.66}$ phase ($\alpha = {}^1/_3$) for different amounts of tetragonal pyramids (*x*) and trigonal bipyramids (*y*) for *x:y* = 4:2 (a), 3:3 (b), and 2:4 (c). (d) Structure of the $Fe_2O_{2.5}$ layer in $Sr_4Fe_6O_{13}$.
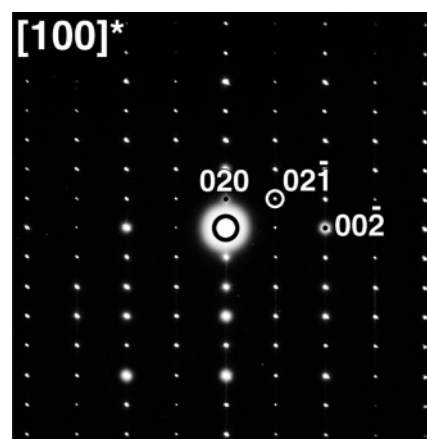
Figure 11. Typical [100]* ED pattern of the $Sr_4Fe_6O_{12.66}$ phase with $\alpha = {}^1/_3$.

bands. This is in agreement with $\alpha = 0.39$, which implies the alternation of approximately nine bands of 5 FeO_5 polyhedra and one band of 6 FeO_5 polyhedra.

3.3.2. Alternation Sequence of the FeO_5 Trigonal Bipyramids and the Square Pyramids and Stacking Sequences of the $Fe_2O_{2+\delta}$ Layers. The exact distribution of the FeO_5 trigonal bypiramids and square pyramids in the $Fe_2O_{2+\delta}$ layers will be analyzed at the next step. Within a certain *n* = 2/α value, given by the α component of the modulation vector, several variants of such distribution with different thicknesses *x* and *y* for the subbands of the tetragonal pyramids and the trigonal bipyramids, respectively, can be realized, if the condition *n* = *x* + *y* is fulfilled. For instance, for the commensurate case of $\alpha = {}^1/_3$, three possible arrangements are shown in Figure 10 for a periodicity of 6 FeO_5 polyhedra (*n* = 6) and a layer composition of $Fe_2O_{2.33}$. The combinations are presented for *x:y* = 4:2 (a), 3:3 (b), and 2:4 (c). Being compared with the $Fe_2O_{2.5}$ layer of the $Sr_4Fe_6O_{13}$ structure (Figure 10d), these possibilities correspond to the evolution of the structure of $Fe_2O_{2+\delta}$ layers

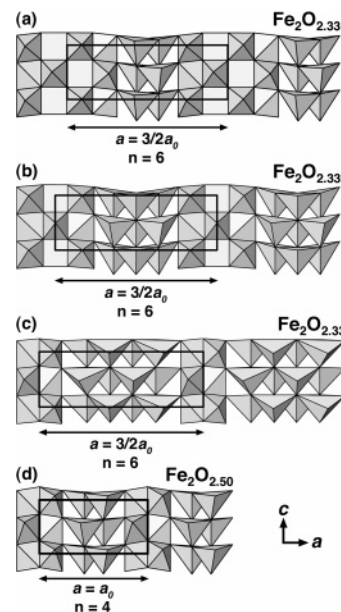by increasing the thickness of the subbands of tetragonal pyramids (*x:y* = 4:2), trigonal bipyramids (*x:y* = 2:4), or growing both subbands in equal amounts (*x:y* = 3:3). The most probable structure for the $Fe_2O_{2+\delta}$ layer can be derived from the [100]* ED pattern of the $\alpha = {}^1/_3$ phase (Figure 11). This most frequently observed pattern shows rows of reflections at the positions 0*kl*, where *k* = even and *l* = odd. The clear 0*kl*, *l* = odd reflections show that the projected potentials at the lattice points separated by *c*/2 are not equal. In Figure 10, it can be seen that the *x:y* = 4:2 and 2:4 structures of the $Fe_2O_{2.33}$ layer will give the same projected scattering density at the points separated by *c*/2. The *x:y* = 3:3 arrangement of Figure 10b, consisting of an alternation of triple bands of square pyramids and trigonal bipyramids, produces the required condition for a nonzero intensity of the 0*kl*, *l* = odd reflections for the $Sr_4Fe_6O_{12.66}$ structure with modulation vector $\mathbf{q} = {}^1/_3\mathbf{a}^*$. The 3D space groups *Ccc*2 and *Cmc*2_1 can be deduced from Table 1 for a commensurate $a = {}^3/_2a_0$, $b = b_0$, $c = c_0$ orthorhombic unit cell. The reflection conditions *hk*0, *h* + *k* = 2*n*, 0*kl*, *k* = 2*n*, 00*l*, *l* =

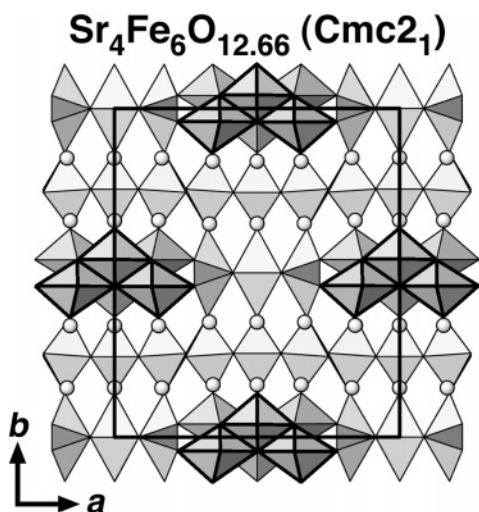**Figure 12.** Structural model for the $Sr_4Fe_6O_{12.66}$ phase with $\alpha = {}^1/_3$ and $Cmc2_1$ space symmetry. Fe atoms are at the octahedral, trigonal bipyramidal, and square pyramidal sites. Shaded circles represent Sr ions.

$2n$ are derived from the [001]* and [100]* ED patterns of the $Sr_4Fe_6O_{12.66}$ structure (Figures 6a and 11, respectively). The $00l$ reflections with $l \neq 2n$ in Figure 11 are weaker than the reflections with $l = 2n$; their intensity vanishes rapidly with increasing tilt angle. The appearance of these forbidden reflections can be attributed to double diffraction. According to these reflection conditions, the $Cmc2_1$ space group can be unambiguously chosen. The structure model for the Sr_4-$Fe_6O_{12.66}$ phase comprising all the features described above is shown in Figure 12. This model will be confirmed when real-space HREM imaging is considered.

A different set of ED patterns corresponding to the $\alpha = {}^1/_3$ case was also occasionally found. The reflection conditions $0kl$, $k + l = 2n$ and $h0l$, $l = 2n$ observed from the [001]*, [010]*, and [100]* ED patterns in Figure 13 do not match the C-centered orthorhombic unit cell and correspond to the space group $Pnc2$, which is a subgroup of $Ccc2$, one of the 3D possible space groups for $\alpha = {}^1/_3$. One can assume that this symmetry decrease occurs due to a change in the stacking sequence of the $Fe_2O_{2.33}$ layers along the b axis. The presence in the [100]* ED pattern of Figure 13 of diffuse streaks along b* indeed indicates the presence of (010) planar defects. A structure model of the $Sr_4Fe_6O_{12.66}$ phase with $Pnc2$ space symmetry is shown in Figure 14. In comparison with the $Cmc2_1$ structure, each second $Fe_2O_{2.33}$ layer is shifted by a $({}^1/_2, 0, {}^1/_2)$ vector of the average unit cell, resulting in a primitive supercell.

The features of the stacking sequence of the $Fe_2O_{2.33}$ layers in the $Cmc2_1$ and $Pnc2$ phases can be observed in the [100] HREM images of Figure 15. Under this particular imaging condition, a zigzag dark pattern, delimited by bright columns of Fe−O atoms, can be easily observed within the $Fe_2O_{2.33}$ layers. The corresponding FT patterns for both images are also included. The upper image shows a well-defined stacking sequence along the b axis corresponding to the $Cmc2_1$ model, with a FT pattern (Figure 15c) identical to the ED pattern in Figure 11. The bottom image presents another stacking sequence (indicated with zigzag white lines) in the $Fe_2O_{2.33}$ layers. It can be easily observed in the zigzag patterns that the $Fe_2O_{2.33}$ layers are shifted over $c/2$ with
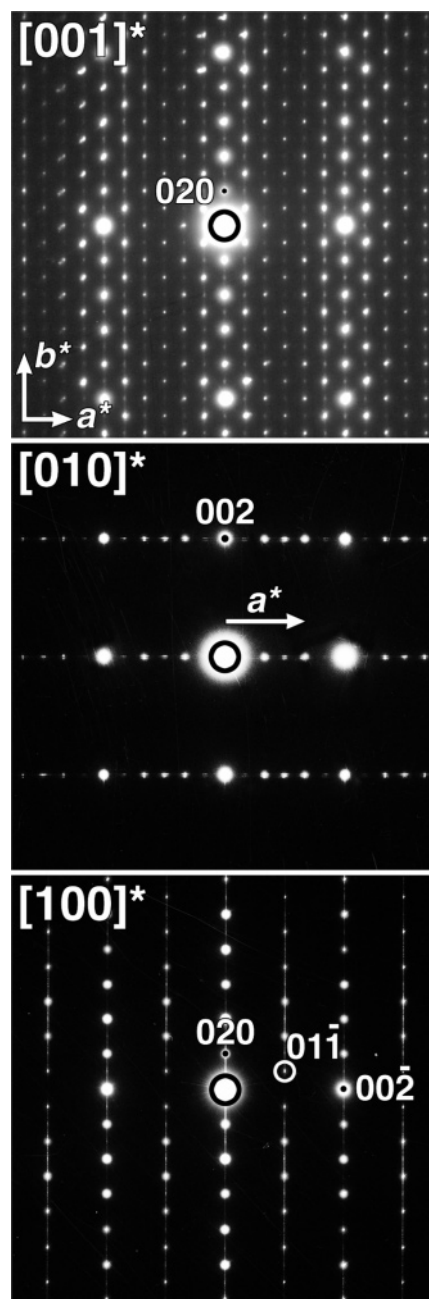

Figure 13. [001]*, [010]*, and [100]* ED patterns of the $Sr_4Fe_6O_{12.66}$ phase with $\alpha = {}^1/_3$ and $Pnc2$ space symmetry.

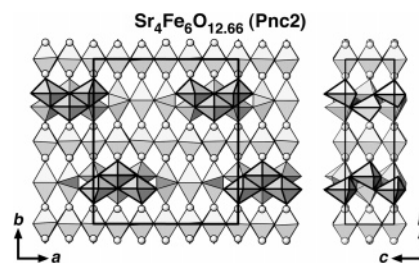**Figure 14.** Structural models for the $Sr_4Fe_6O_{12.66}$ phase with $\alpha = {}^1/_3$ and $Pnc2$ space symmetry. Fe atoms are at the octahedral, trigonal bipyramidal, and square pyramidal sites. Shaded circles represent Sr ions.

respect to the adjacent layers. The FT pattern taken from this image (Figure 15d) is identical to the [100]* ED pattern of the $Pnc2$ structure (Figure 13). Stacking disorders are present, as are pointed out by arrowheads, and can be interpreted as thin slabs of the $Cmc2_1$ structure in the $Pnc2$
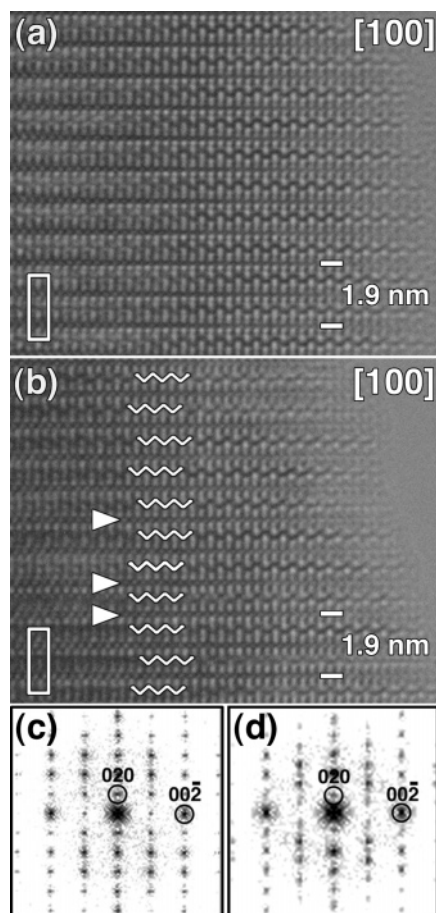
Figure 15. [100] HREM images of the $Sr_4Fe_6O_{12.66}$ phase: (a) typical stacking sequence corresponding to the $Cmc2_1$ space symmetry; (b) stacking sequence of the $Pnc2$ phase; (c and d) corresponding FT patterns of the $Cmc2_1$ and $Pnc2$ phases, respectively. The zigzag lines mark the positions of the $Fe_2O_{2.33}$ layers. The arrowheads show stacking faults that can be interpreted as thin slabs of the $Cmc2_1$ structure in the $Pnc2$ matrix. The unit cells are outlined by white rectangles in both images.

Figure 16. [100] HREM image showing the presence of a nanoslab of $SrFeO_{3-\delta}$ perovskite within the $Sr_4Fe_6O_{12+\delta}$ material and corresponding ED pattern. The reflections outlined by white circles are due to the perovskite.

matrix. Such defects are responsible for the diffuse intensity lines along b^* observed on the [100]* ED patterns of the $Pnc2$ phase. Also, nanosized slabs of $SrFeO_{3-\delta}$ perovskite with highly variable thickness (from 2 to 40 perovskite blocks) are sometimes present as an intergrowth within the $Sr_4Fe_6O_{12+\delta}$ material (Figure 16). The ED pattern in Figure 16 is a superposition of the patterns from $Sr_4Fe_6O_{12+\delta}$ and the perovskite. More intense reflections belong to the $Sr_4Fe_6O_{12+\delta}$ compound, whereas the weaker ones are due to the perovskite. The following epitaxial relations are found: $[001]_P||[010]_{SFO}$ and $(110)_P||(001)_{SFO}$ (where P is perovskite).

The $Cmc2_1$ and $Pnc2$ structure models were verified by calculations of theoretical [100] HREM images. Simulated images based on both models are shown in Figure 17 and have good agreement with the experimental HREM images.

Using a consideration of geometrical mismatch between the perovskite-type layers and the $Fe_2O_{2+\delta}$ layers, Mellenne et al.[10] came to the conclusion that the evolution of the structure of the $Fe_2O_{2+\delta}$ layers with decreasing δ involves preferentially the addition of extra tetragonal pyramids. They argued that an increase of the thickness of the trigonal bipyramids subband would be difficult or may be impossible to stabilize due to the large mismatch with the perovskite block. Our XRPD investigation showed that decreasing δ
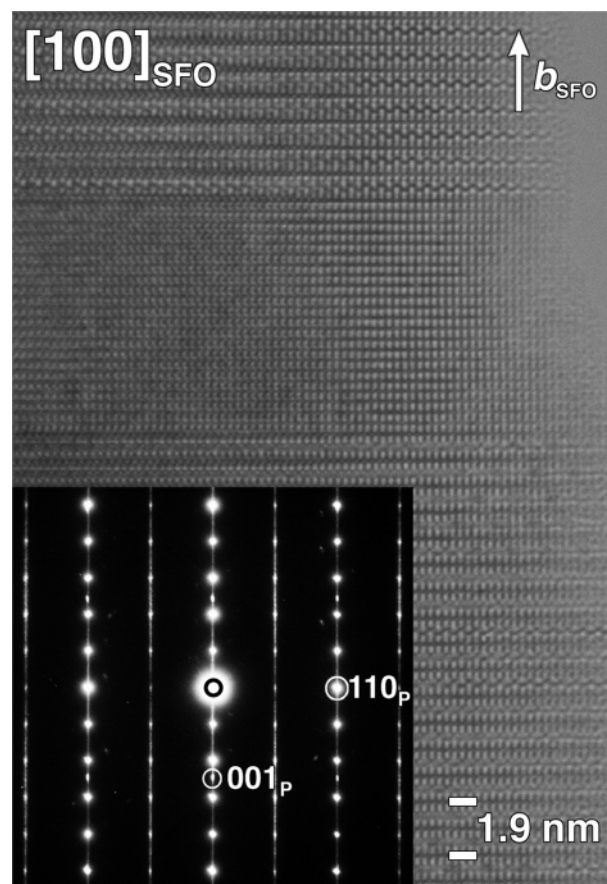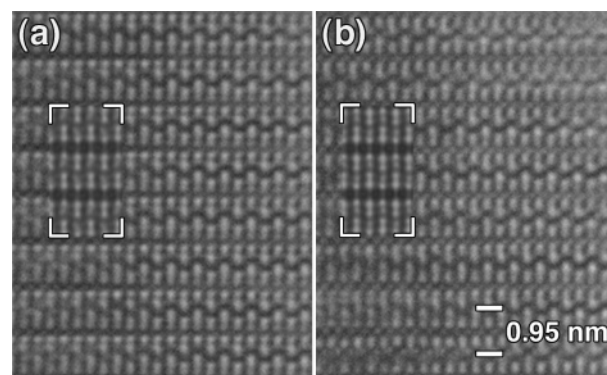

Figure 17. [100] HREM image and calculated images based on the $Cmc2_1$ model (a) and $Pnc2$ model (b) for a defocus value $\Delta f = -75$ nm and a thickness $t = 5.5$ nm.

from 1.0 to 0.8 results in a simultaneous noticeable decrease of the $^1/_2a_0$ parameter from 5.5515 to 5.5245(2) Å. When it is taken into account that, according to Mellenne et al.,[10] the introduction of extra trigonal bipyramids favors the decrease of the cell parameter, this fact is not in agreement with the hypothesis about a preferential growth of the tetragonal pyramid subband. Our HREM observations favor the mechanism where both the tetragonal pyramid and trigonal bipyramid subbands grow in nearly equal amounts, which increases the probability of compensation of the stress caused by the different sizes of the two types of FeO_5 polyhedra.

4. Conclusion

As a conclusion, some comments should be addressed to the influence of the misfit strain on the structure when the $Sr_4Fe_6O_{12+\delta}$ material is prepared as an epitaxial thin film. Indeed, the possibility to prepare such bulk materials shows that the requirement of the misfit accommodation is not absolutely necessary for the stabilization of such a reduced structure. On the other hand, the comparative TEM investigation of the $Sr_4Fe_6O_{12+\delta}$ material in thin film and bulk forms reveals that the former was more uniform with respect to the anion content and the related superstructures, whereas the bulk material was significantly more disordered. One can assume that the misfit strain plays an important role in the preferential formation of a $Sr_4Fe_6O_{12+\delta}$ phase with certain α and δ values, which allows better accommodation of the stress in comparison with the others. This assumption might open a route for a controlled preparation of the $Sr_4Fe_6O_{12+\delta}$ phases with a required oxygen content by choosing the appropriate material for the film substrate.